Research Article

Numerical investigation of nanofluid heat transfer in the wall cooling panels of an electric arc steelmaking furnace

Milad Babadi Soultanzadeh[1,2] · Mojtaba Haratian[2] · Babak Mehmandoust[2] · Alireza Moradi[2]

© The Author(s) 2023   OPEN

Abstract

Wall cooling panels are typically a kind of electric arc furnace equipment that has precisely influence on different aspects of the steelmaking process. This investigation employs a CFD method to evaluate the thermal performance of water cooling panels in real operating conditions to validate the numerical method followed by replacing cooling water with Al_2O_3/Water nanofluid coolant. The results are revealed that the high rate of receiving heat flux and generated vortexes with low-velocity cores lead to hot spots inducing on bends and elbows. In the operating flow rate, the maximum temperature of the hot-side wall decrease by 14.4% through increasing the nanoparticle concentration up to 5%, where the difference between maximum temperature and average temperature on the hot-side decrease to 12 degrees. According to the results, use of nanofluid coolant is a promising method to fade the hot spots out on the hot-side and gifting a lower and smoother temperature distribution on the panel walls of thereby prolonging the usage period of panels.

Article highlights

- Receiving radiative heat flux of a water cooling panel (WCP) of an Electric Arc Furnace (EAF) is calculated numerically using the S2S model.
- Temperature distribution and hot spots is determined on the outer wall of CWP.

- Heat transfer of WCP is characterized numerically for Al_2O_3/Water nanofluid at various particle concentrations.
- Smoothing temperature distribution and hot spot removal are dedicated as the results when using nanofluid.

List of symbols

A	Surface area (m^2)
$C_{P_{bf}}$	Isobaric specific heat capacity base fluid (J/kg K)
$C_{P_{nf}}$	Isobaric specific heat capacity nanofluid (J/kg K)
$C_{P_{np}}$	Isobaric specific heat capacity nano particles (J/kg K)
CP	Cooling panel
EAF	Electric arc furnace
F	View Factor in radiative heat transfer
g_i	Gravitational acceleration in ith direction (m/s^2)
h	Convective heat transfer coefficient (pure base fluid) (W/m^2 K)
h_{eff}	Convective heat transfer coefficient of nanofluid (W/m^2 K)

✉ Milad Babadi Soultanzadeh, milad.babadisoultanzadeh@mail.concordia.ca; ✉ Mojtaba Haratian, haratian@iaukhsh.ac.ir | [1]Department of Building, Civil and Environmental Engineering, Concordia University, Montreal, Canada. [2]Department of Mechanical Engineering, Khomeinishahr Branch, Islamic Azad University, Isfahan, Iran.

K_{bf} Thermal conductivity of base fluid (W/m K)
K_{nf} Thermal conductivity of nanofluid (W/m K)
K_{np} Thermal conductivity nano particle (W/m K)
Nu   Nusslet number
p   Reflectivity
P   Pressure (Pa)
Pr   Prandtl number
q   Heat flux (W/m^2)
q_{in} Incident heat flux by hot side (W/m^2)
q_{out} Leaving heat flux by molten steel (W/m^2)
Re_D Reynolds number with the characteristic length of WCP inner diameter
T   Temperature (K)
S_R Energy source term (J/m^3)
u_i Velocity component in ith direction (m/s)
WCP   Wall cooling panel
x_i The ith direction in the Cartesian coordinate system (m)

Greek Letters

δ_{ij} Kronecker delta
ε_k Emissivity of kth component
σ Stefan–Boltzmann constant (W/m^2 K^4)
σ_T Turbulent Prandtl number
ϕ Nanofluid concenteration
ρ Density (kg/m^3)
ρ_{bf} Base-fluid density (kg/m^3)
ρ_{nf} Nanofluid density (kg/m^3)
ρ_{np} Nano particle density (kg/m^3)
μ Viscosity (Pa s)
μ_t Turbulent viscosity (Pa s)
μ_{bf} Base-fluid viscosity (Pa.s)
μ_{nf} Nanofluid viscosity (Pa s)

1 Introduction

Generally, the new generation of electric arc furnaces (EFA) includes a circular wall which is protected by a refractory brick liner, a cupped bottom bath and a circular detachable roof protected by roof water cooling panels. The walls of EAF are usually cylindrical and are made of different materials, depending on whether the furnace is acidic or alkaline to have been protected by Water cooling panels similar to the roof [1]. These cooling panels (CP) experience conflicting operational situations [2]. CPs are usually damaged on the outer side upon receiving heat flux and significant thermal stresses, and on the inner side through corrosion and erosion caused by circulating cooling water, which delays the production process [3, 4]. Regarding the previous investigations on the thermal performance of nanofluids, use of these specific types of fluids as circulating cooling fluids leads to diminished exterior walls

temperature of CPs which reduces thermal stress and improves productivity [5].

Kilkis et al. [6] presented a simplified analytical one-dimension model to study radiative and conductive heat transfer in EAF whose results matched numerical simulations which were usable in the design and evaluation of EAF. Radiative heat transfer modelling continued by Logar et al. [7] by applying a surface to surface model to simplified EAF. Their results revealed geometry simplification had a negligible effect on the simulation results and applied numerical results was in accordance with measured operational data. Studies were extended by Henning et al. [8] with CFD evaluation roof CP of AC and DC EAF using STAR-CCM+ commercial code as well as experimental studies by liberator prototyping which showed a good agreement between CFD and experimental results. They also find out that temperature of internal walls of tubes may increase up to 100 C caused by cooling water low velocity which can be solved by increasing water flow rate. Mombeni et al. [9] examined transient flow and heat transfer in EAF roof CP using CFD and presented an improved geometry for roof CP. Their results revealed that using cooper instead of steel can reduce maximum temperature of CP up to 6% and replacing roof CPs with circular panels will make temperature distribution smoother. They also showed that hot spots occurred near the elbows. CFD simulations were pursued by Yigit et al. [10] to examine temperature distribution in an EAF with active burner and electrodes by considering combustion reaction and radiative heat transfer. They examined temperature distribution on walls and slag surface inside an EAF using CFD techniques. Their results indicated that walls and roofs received more thermal enegy with comparison of slag surface and the cooling system is responsible for significant heat losses in EAF. Guo et al. [11] inspected the radiation intensity and influence of arc length on heat flux distribution in EAF using CFD. They resulted 0.3–2% heat loss in electrodes due to conductive heat transfer. Also they estimated maximum temperature on the electrodes 3600 K that is not reasonable. Khoda-bandeh et al. [12] characterized heat transfer phenomena in oxidizer lances of EAF, both numerically and experimentally. They applied DO (Discrete Ordinate) method in radiative heat transfer to examine the heat transfer phenomena. Their results show that 180 degree elbows causing returned vortex in pipeline and increase the local temperature which headed them to improve water-cooled oxidizer lances. They also find out that thermal gradient in EAF is a source of fatique and thermal stress. Khoda-bandeh et al. [13] proceeded with a parametric study of EAF cooling system by applying CFD. For numerical formulation they employed S2S radiative heat transfer model. They validated CFD results by comparing them against the outlet water temperature of CP and revealed the effect

of slug thickness on CP outer wall temperature distribution. Their results also revealed that increase in EAF diameter will lead to higher temperature on roof and lower temperature on side walls. Besides, they found out that cooling pipes experience high temperature gradient on bending which may casus the mechanical failure. Ahmadi et al. [14] optimized roof cooling panels of EAF by using nanofluid as the cooling fluid. They employed numerical simulations using ANSYS Fluent and compared the results for pure water and 3% and 5% nanofluid concentration. They considered outer walls as constant heat flux applying boundary. Their results show that the internal walls temperature decreased by increasing in Reynolds number and concentration. Yao et al. [15] developed a 2D numerical simulation using ANSYS Fluent to examine molting bath cavity in a DC EAF. They realized two clockwise and counter clockwise flow patterns formed in the molten bath. In addition, their results show high temperature region in surface of molten bath caused by the plasma sear stress. Luo et al. [16] employed ANSYS Fluent for numerical simulations to evaluate effect of EAF on water CP overheating. P1 heat transfer radiation and transport species models are used by them. Their numerical results show that decrease in molten bath and increase in water cooling flow rate as well as decrease in arc power are needed to avoid overheating of the CPs.

A nanofluid is a mixture of a base fluid and a small volume fraction (Concentration) of solid particles with dimensions less than 100 nm within the range of sub 1% to 10% [17]. In comparison with conventional fluids, nanofluids have high thermal conductivity and can transfer heat more effectively through the convective heat transfer mechanism. While there are many types of nanofluids, mixtures of Al_2O_3 and Water are more effective at higher concentration values and can be considered as a Newtonian fluid up to 5% concentration [18]. To improve the thermal performance of various types of heat transfer components, Al_2O_3/Water nanofluids were used since geometrical modifications are costly and sometimes impossible [19].

Since the possible use of nanofluids in the cooling system of EAF has been investigated rarely so far and considering that wall CP is principally a heat exchanger, the following cases with various similar applications have been adequately reviewed. Islam et al. [20] improved fuel cell cooling system using nanofluid as a coolant fluid operating through a compact heat exchanger. Their results showed that an increase in the nanoparticle concentration led to heat transfer improvement. Sahota et al. [21] explored the thermal performance of a helically coiled solar collector using two different types of nanofluids and showed improved energetic and exergetic efficiency. Nanofluid applications in a high rate heat flux cases were tested by Nayerdinzadeh et al. [22]. That evaluated

parabolic through the solar collector using nanofluid both numerically and experimentally. Their results revealed that while heat transfer coefficient rose by increasing the nanoparticle volume fraction, the elevation of the friction coefficient was negligible. Hosseini et al. [23] evaluated nanofluid performance as a coolant fluid in a shell and tube intercooler using ASPEN HTFS* commercial software and confirmed previous results.

In the present investigation, computational fluid dynamics methods were employed to carefully evaluate the thermal performance of a WCP in an EAF which employs Al_2O_3/Water nanofluid as a circulating cooling fluid. One of the significant critical aspects of this study is marking and fading away hot spots on the outer hot-side of CP as well as reducing the average temperature of outer CPs hot-side. Numerical investigation was conducted on an Isfahan steel factory EAF WCP. Initially, CFD simulations were verified by comparing them against operating data exported from the monitoring system under identical specific conditions using cooling water as a coolant. In the second step, pure water was replaced by Al_2O_3/Water nanofluid with 3%, 4%, and 5% particle volume concentrations.

In the next section, we consider the methodology that includes geometry and mesh generation, Governing equations, and Boundary conditions. Section 3, provides the results and discussion that also include the validation and the mesh independency study. Finally, in Sect. 4, we present the conclusion.

2 Methodology

This study conducted CFD simulation in the two divided parts to EAF WCP: in the first place WCP receiving heat flux was calculated under identical operating conditions based on simplified EAF geometry produced by CATA V.5. According to [7], geometry simplification has a negligible influence on final results. Mesh generation and CFD simulations were done using GAMBIT and ANSYS FLUENT 19 commercial code, respectively. Since radiative heat transfer mechanism claims the most sizeable share of heat transfer in EAF, other heat transfer mechanisms were neglected. Also, S2S radiant model was employed to model radiant heat transfer between the hot molten steel surface and WCP hot-side. At this stage, based on identical operating conditions, it was reasonably assumed that the electric arc was offed for a while and electrodes had been lifted up. In addition, molten steel was still static in the furnaces' bath. Also, a WCP was placed in the wall of circular furnaces while the rest of the wall was assumed to realistically be at a constant temperature equivalent to the panel surface. Further, regarding to Isfahan steel factory surface temperature and emissivity

of molten steel assumed 1600 centigrade and 0.63, respectively. On the other hand, numerical simulations were done in a steady state to achieve the spatial heat flux distribution on the hot-side of WCP and validated against the operating empirical data. In the second part of the simulation, the validated spatial heat flux distribution was applied as a heat flux profile to the hot-side of WCP in order to simulate the internal flow and heat transfer to the cooling fluid. Initially in this part, pure water with an empirical operating flow rate was considered as coolant to validate the results against the outlet temperature [5]. Next, simulations were conducted on pure water and 3%, 4% and 5% particle concentrations of Al_2O_3/Water nanofluid at 9, 10 (nominal flow rate), 11 and 12 kg/s flow rates. It is predicted that low concentration of nanoparticles will not demonstrate any significant improvement due to the immense values of flow rates. The proposed nanoparticle properties, WCP material (ASTM A106 GR.B), and nanofluid calculated thermophysical properties are presented in Tables 1, 2, 3 respectively. A flowchart of methodology steps was dedicated to Fig. 1 to make it easier to understand the simulation steps.

2.1 Geometry and mesh generation

Since in the first part of the simulation to calculate the receiving heat flux on hot-side of WCP, electric arc is assumed to be offed, the sole source of heat energy is hot molten steel through the furnaces path. The geometry for the first part is depicted in Fig. 2. In addition, WCPs geometry and dimensions reported by Isfahan Steel Factory for the second simulation part are presented in Fig. 3.

The geometric properties of EAF and WCP are presented in Table 4.

Figure 4 illustrates the generated grid on the domain walls and Fig. 5 outlines a planar view of the internal grids indicating a higher resolution near the WCPs wall. Further, Fig. 6 displays the mesh generated for the second simulation part which includes the internal flow and heat transfer.

Table 1 Nanoparticle properties

Property	Value
Chemical formula	Y-Al_2O_3
Nano powder color	White
Shape	Spherical
Averaged diameter	20 nm
Specific surface area	128 m^2/g
Density	3.89 g/cc
Heat capacity	880 J/kg K
Purity	99%

Table 2 Thermophysical properties of WCP pipes

Property	Value
Pipe	ASTM A106 GR.B
Thermal conductivity	51 W/mK
Specific heat capacity	461 J/kgK
Density	7850 kg/m^3

Table 3 Calculated thermophysical properties of Al_2O_3/water nanofluid

Particle concentration	3%	4%	5%
Density (kg/m^3)	1074.909	1101.869	1128.829
Specific Heat Capacity (J/kgK)	3829.222	3723.949	3623.706
Viscosity (Pa s)	0.000776	0.000797	0.000818
Thermal conductivity (W/mK)	0.763006	0.809568	0.85613

For both simulations, an unstructured pyramidal gird was employed, and four grid resolutions were adequately studied in order to properly investigate mesh independency. The numbers of cells studied for the first and second parts of simulations are 454,123, 491,231, 540,133, 601,234; and 912,314, 1,042,341, 1,131,806, 1,326,871, respectively.

2.2 Governing equations

The governing equations are classified into three classes:
(i) fundamental equations of S2S radiative heat transfer that govern the heat transfer outside the WCP and result heat flux distribution on the WCPs outer hot-side Eqs. 1–5 [24].

$$q_{out,k} = \sigma T_k^4 + p_k q_{in,k} \tag{1}$$

$$A_k q_{in,k} = \sum_{j=1}^{n} A_j q_{out,j} F_{jk} \tag{2}$$

$$A_j F_{jk} = A_k F_{kj} \quad \text{for } j = 1, 2, 3, \dots N \tag{3}$$

$$q_{in,k} = \sum_{j=1}^{N} F_{kj} q_{out,j} \tag{4}$$

$$F_{ij} = \frac{1}{A_i} \int_{A_i} \int_{A_j} \frac{\cos \theta_i \cos \theta_j}{\pi r^2} \delta_{ij} dA_i dA_j \tag{5}$$

In these equations, $q_{out,k}$ is leaving energy flux from kth surface which is calculated by composing directly emitted and reflected energy. Also, ε_k, σ, p_k and $q_{in,k}$ are emissivity,
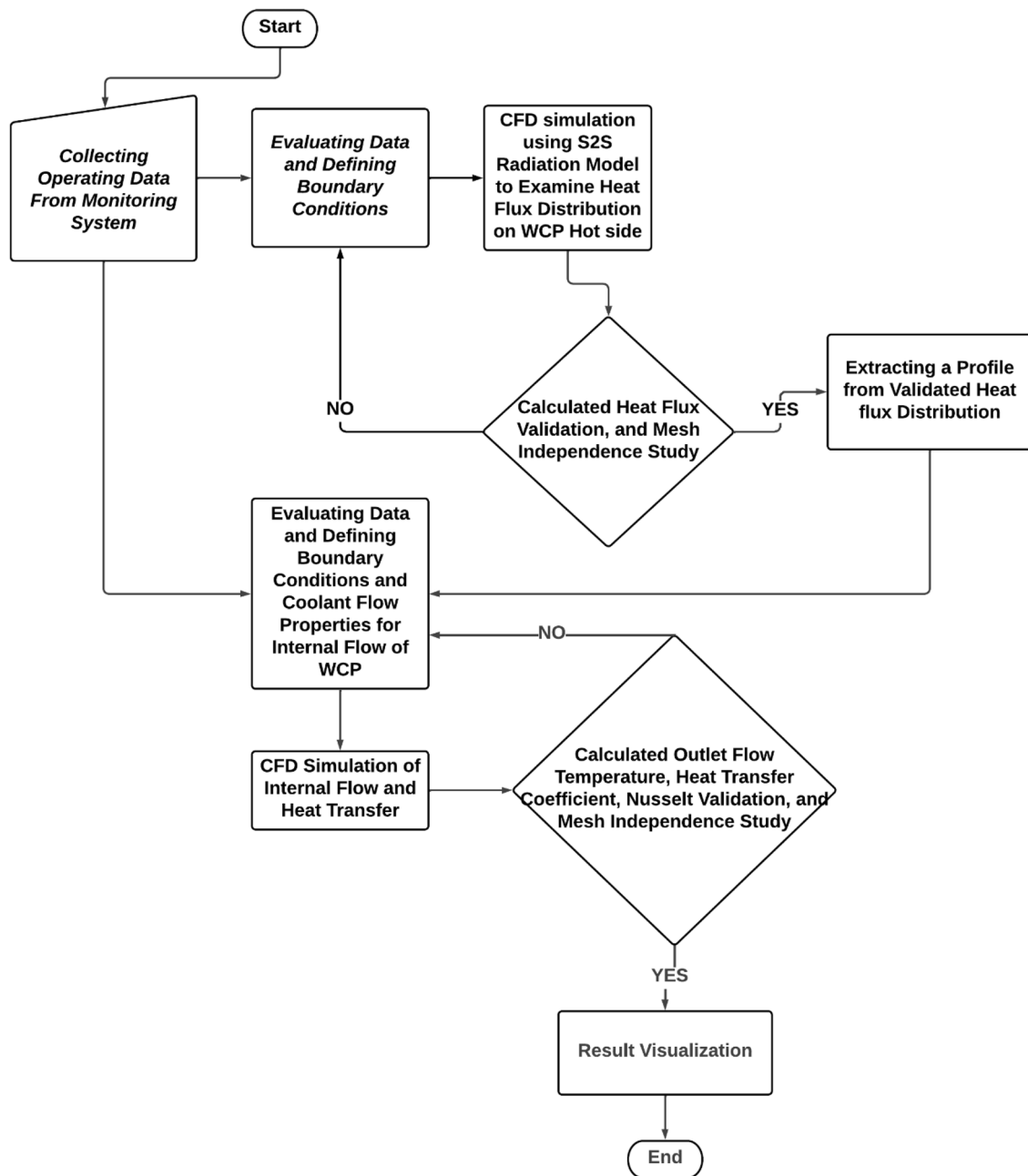
Fig. 1 Schematic flow chart of the methodology

Stefan–Boltzmann constant, reflectivity and incident energy flux for kth surface. F defined as surface to surface view factor and A is are of the surfaces.

(ii) Internal flow and heat transfer inside the WCP are provided in Eqs. 6–12 [9, 24].

Continuity and momentum equations dedicated in Eqs. 6 and 7, respectively.

$$\frac{\partial}{\partial u_i}(\rho u_i) = 0 \tag{7}$$

$$\frac{\partial}{\partial x_i}(\rho u_i u_j) = -\frac{\partial P}{\partial x_i} + \frac{\partial}{\partial x_i}[(\mu_t + \mu)(\frac{\partial u_i}{\partial x_j} + \frac{\partial u_j}{\partial x_i}) - \frac{2}{3}(\mu_t + \mu)\frac{\partial u_l}{\partial x_l}\delta_{ij}] + \rho g_i \tag{8}$$

Fig. 2 EAF Geometry and the location of WCP
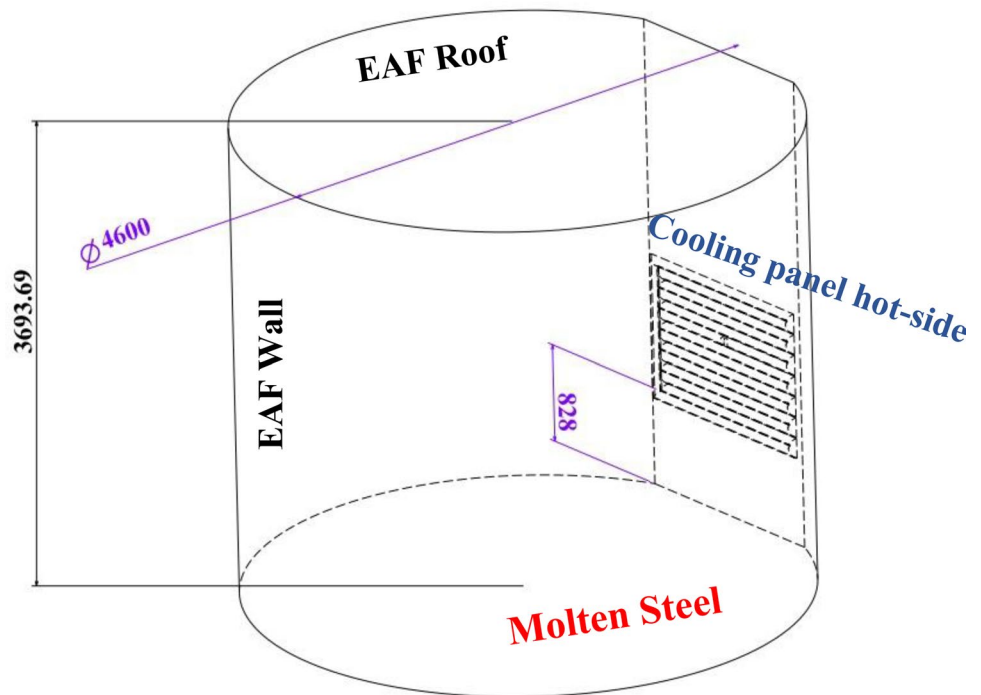
Fig. 3 Geometry of wall water cooling panel (WCP)
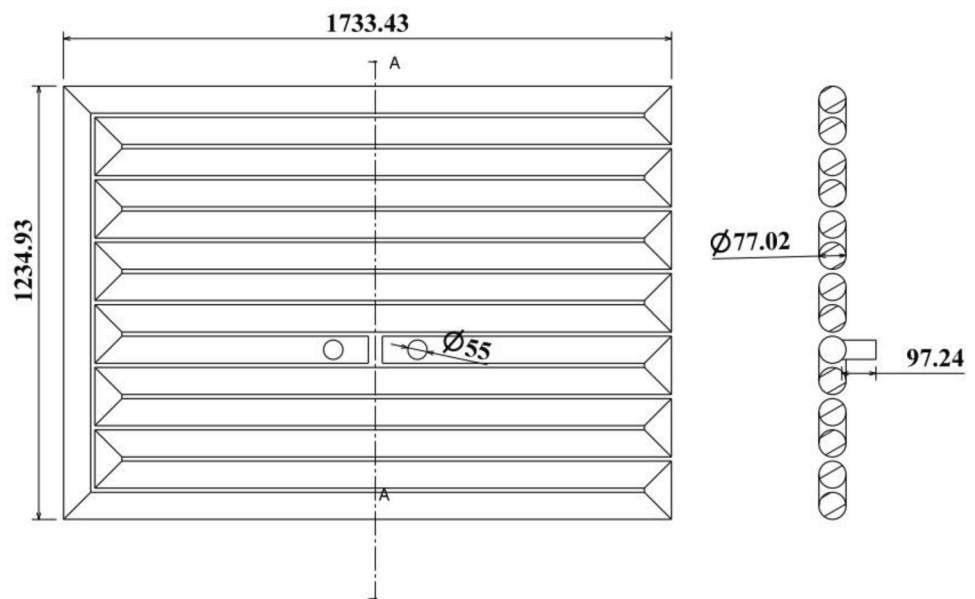
Table 4 Geometrical dimensions of EAF and WCP

Parameter	Value
EAF diameter	4.6 m
EAF roof distance from molten steel	3.3639 m
WCP distance from molten steel surface	0.828 m
WCPs inlet and outlet inner diameter	55 mm
WCPs pipes inner diameter	77.02 mm
WCPs pipes thickness	5.49 mm
WCP dimensions	1.73344*1.23493 m^2

where the ρ, u_i and P are density, velocity component and pressure, respectively. Also, μ_t, μ, δ_{ij} and g_i are turbulent viscosity, laminar viscosity, Kronecker delta and gravitational acceleration component, respectively.

Energy equation defined as Eq. 8:

$$\frac{\partial}{\partial x_i}(\rho u_i T) = \frac{\partial}{\partial x_i}\left[\left(\frac{\mu}{\mathrm{Pr}} + \frac{\mu_t}{\sigma_T}\right)\frac{\partial T}{\partial x_i}\right] + S_R \tag{8}$$
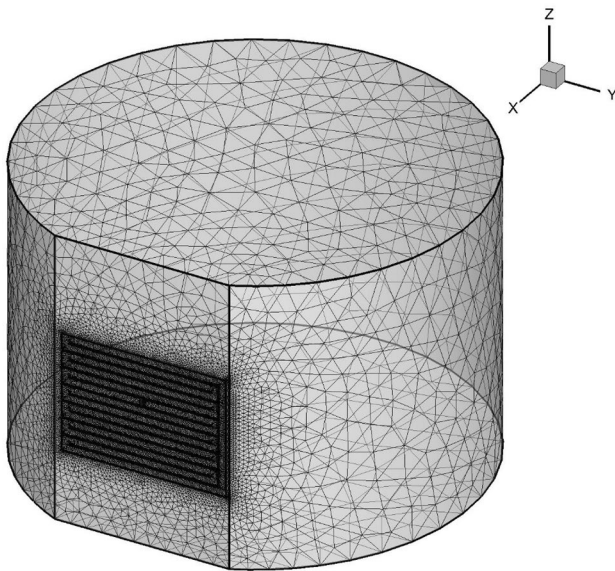
Fig. 4 Generated grid for first step (receiving heat flux) simulation on the boundaries of domain
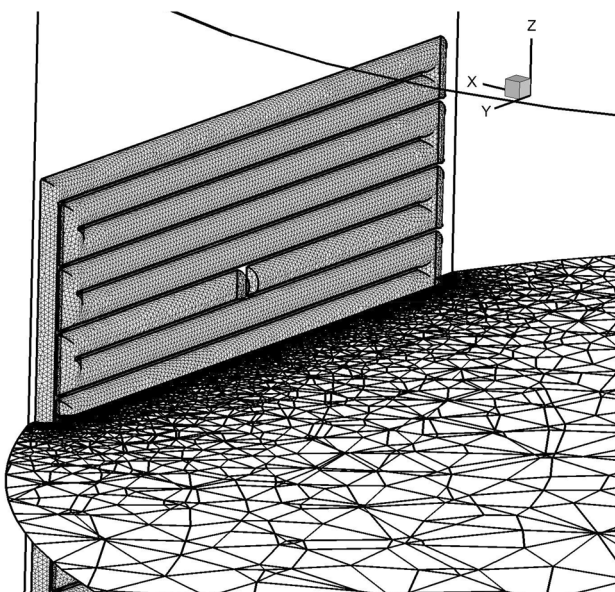
Fig. 5 Planar view of generated grid inside the EAF domain in first step (receiving heat flux) simulation

In this equation T is the temperature, Pr is Prandtl number, σ_T and S_R are turbulent Prandtl number and energy source term, respectively.

In addition, realizable k–ε model has been considered in order to model the turbulent flow regime. Realizable k–ε model meets certain mathematical constraints on Reynolds stress, which correspond to turbulent flow physics [16]. Furthermore, compared to the standard k–ε model, the realizable k–ε model shows significant

improvements in streamline curvature, vortices, and rotation features. Also, different Studies of flows with complex secondary flow features have shown that the realizable k-ε model performs best among all the k–ε models [24]. Due to the complex vortices and secondary flow features in the bends of WCP, this model has been employed in the recent investigation.

(iii) equations of nanofluid properties governing the thermophysical properties of nanofluid function of volume concentration in Eqs. 9 to 12 [5, 25]. In the following equations thermophysical properties have been considered temperature independent.

$$\rho_{nf} = \rho_{bf}(1 - \varphi) + \rho_{np}\varphi \tag{9}$$

$$C_{p_{nf}} = \frac{\rho_{nf}(1 - \varphi)C_{p_{bf}}}{\rho_{nf}} + \frac{\rho_{np}\varphi C_{p_{np}}}{\rho_{nf}} \tag{10}$$

$$K_{nf} = \frac{K_{np} + 2K_{bf} + 2\varphi(K_{np} - K_{bf})}{K_{np} + 2K_{bf} - \varphi(K_{np} - K_{bf})} \tag{11}$$

$$\mu_{nf} = \frac{\mu_{bf}}{(1 - \phi)^{2.5}} \tag{12}$$

where the φ is concentration and defines as ratio of nanoparticles volume to the total volume of nanofluid. Besides in all equations np, bf and nf indices reference to nanoparticle, base fluid and nanofluid respectively. ρ, C_p, K and μ represent the density, isobaric specific heat capacity, thermal conductivity and viscosity, respectively.

2.3 Boundary conditions

Since simulation has been done in two steps, specified different boundary conditions have been set corresponding to each simulation. Although for the first step all of the boundaries including WCPs outer hot-side, furnace walls, and molten steel, assumed solid walls due to using S2S model, varying types of boundaries were set in the second step as presented in Fig. 7. In this regard, Table 5 reports all boundary types and identical values used for each step of the simulation. This is valuable to notice that the average temperature on the hot side of the WCP has been reported by factory data for the 10.0407 kg/s flow rate. However, any change in flow rate may cause affect this temperature and incident heat flux. Regarding the radiative heat transfer equations (Eqs. 1–5), 10 degrees change in the average temperature of WCPs hot side leads to a 0.0115% increment in the incident heat flux which is negligible. As a result of the molten steel's temperature being significantly higher than that of the WCP, this occurred.

Fig. 6 Generate grid in second step (WCP internal flow) domain; **A** cross section of WCP pipes, **B** symmetrical plan of WCP and **C** WCP walls

3 Results and discussion
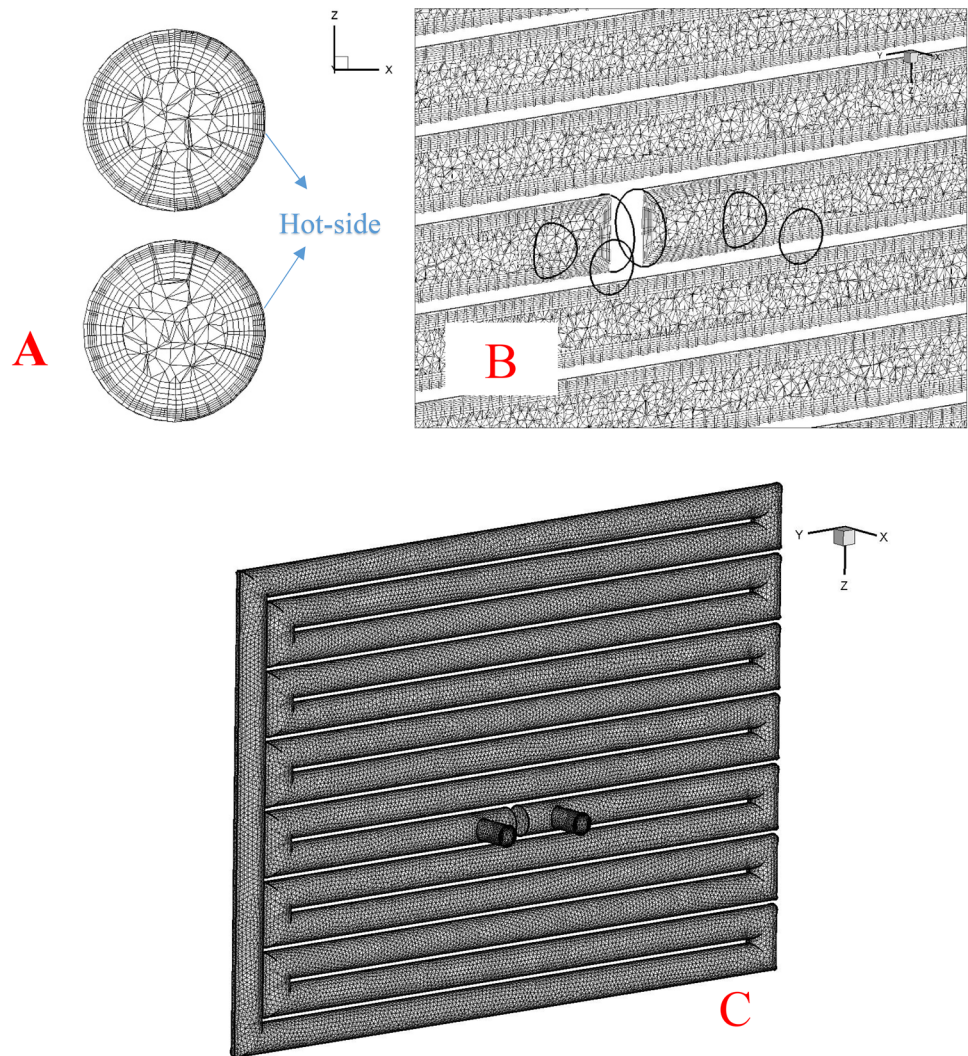
For the internal flow (second step) simulation, WCPs wall was divided into two separated hot-side and cold side. Indeed, the cold side is towards the refractory bricks experiencing no radiative heat flux; thus it is far colder than hot-side which experiences a significant amount of heat flux. The calculated heat flux results of the first step were applied as a profile to the hot-side and convective heat transfer coefficient equivalent to 3 W/m² was applied to the cold side [9]. The free stream temperature around the panels was set 50 °C based on the operating condition. The geometry of the WCP was defined as inner diameter and outer wall diameter modeled as the shell conduction model with 5.49 mm thickness. The shell conduction model typically calculates the outer wall temperature solving the conduction heat transfer equation.

Initially, various simulations were performed to study grid independency under the corresponding empirical operating conditions. Generally, the operating WCP mass flow rate should be higher than 9 kg/s [1]. However, the monitoring system reported 10.0407 kg/s flow rate under the mentioned condition. Figures 8 and 9 illustrate the average receiving heat flux on the WCP hot-side and maximum temperature induced on the outer hot-side versus the number of grid cells, respectively. Although the number of cells increased considerably, the value of heat flux remained almost constant and the difference in the maximum temperature was less than 0.4% from the lowest cell numbers to the highest one. To make the computational cost reasonable, the grid with 540,133 cells has been selected for the first part of simulation. The deviation of average heat flux received by hot side of CWP for the grid with 540,133 cells and the grid with 601,234 cells
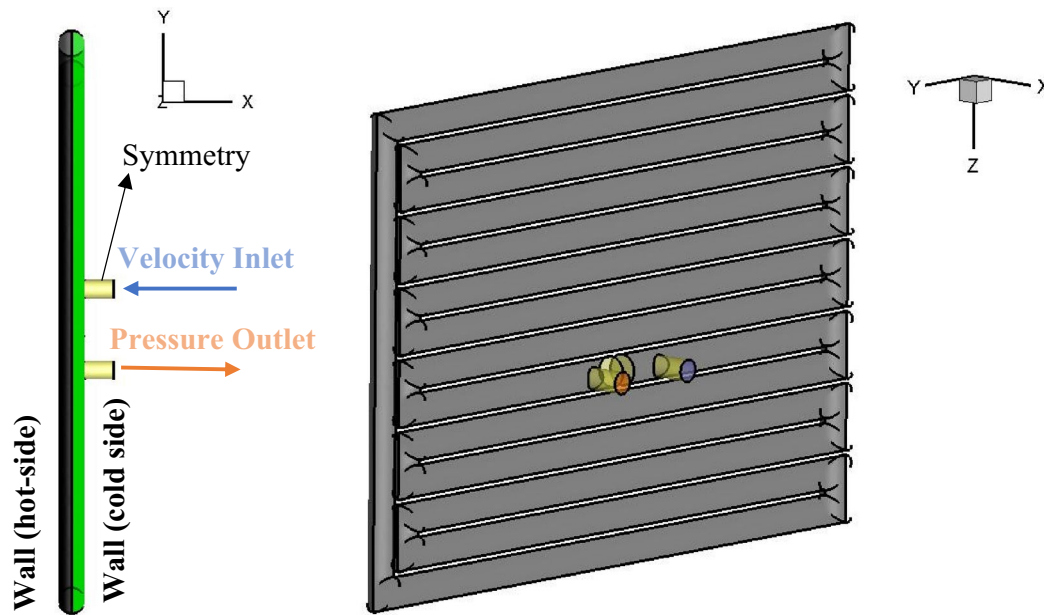
Fig. 7 Boundary conditions for second step (WCP internal flow) simulation; Blue: velocity inlet, Red: pressure outlet, Yellow: symmetry, Gray: wall

Table 5 Boundary conditions

Boundary	Condition	Value
Receiving heat flux simulation (first step)		
WCPs hot-side	Wall	Constant temperature 60 Celsius regarding empirical condition
Molten steel surface	Wall	Constant temperature 1600 Celsius regarding empirical condition
EAF roof and wall	Wall	Constant temperature 60 Celsius regarding empirical condition
WCP internal flow simulation (second step)		
WCP inlet	Velocity inlet	Regarding mass flow rate 9–12 kg/s; 30.527 Celsius regard to empirical condition
WCP outlet	Pressure outlet	Gauge pressure = 0
Wall inlet and outlet	Symmetric	–
WCP hot-side	Wall	Receiving heat flux profile
WCP cold side	Wall	Convective heat transfer h = 3 W/m^{2}K and T$_{sur}$ = 50 Celsius

has been calculated less than 0.004%. In the same aspect, maximum temperature on hot side calculated by the grid with 1,131,806 cells show less than 0.015% deviation from the grid with 1,326,871 cells. Consequently, for the second part of the simulation, the grid with 1,131,806 has been employed for comprehensive simulations.

On the other hand, the heat flux received was calculated 103,677 W/m^2 while it was measured 99,662 W/m^2 under real empirical conditions. In this regard, Mombeini et al. [9] reported 108,236 W/m^2 for receiving heat flux. Thus, comparison of the heat flux reported in the present study, measured data, and previous work [9] validated the simulation results. According to Fig. 10, the differences

between calculated and measured heat flux are less than 4%.

Likewise, validation by Khodabandeh et al. [13] using the outlet temperature versus real empirical data for pure water flow showed practically complete covering with numerical simulations. Studies have also compared to modified Pak and Cho [26] correlation for nanofluids. According to [26, 27], the average error in this experimental equation is function of Reynolds number. However, based on Fig. 11, Reynolds number increment led to decreased divergence for the nanofluid at all particle concentrations. Also, at a constant Reynolds number, the
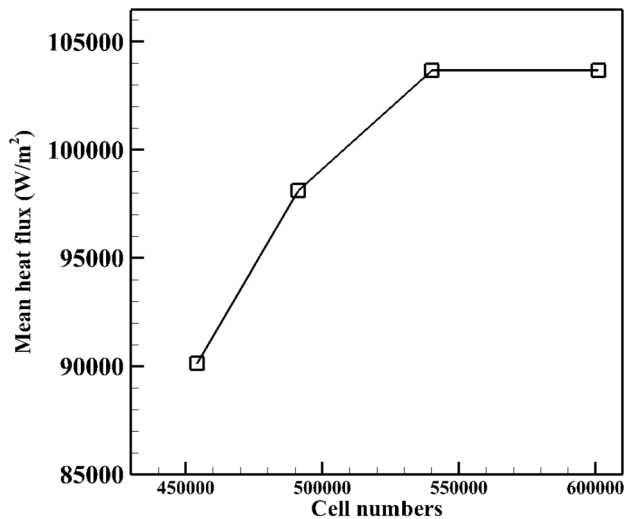
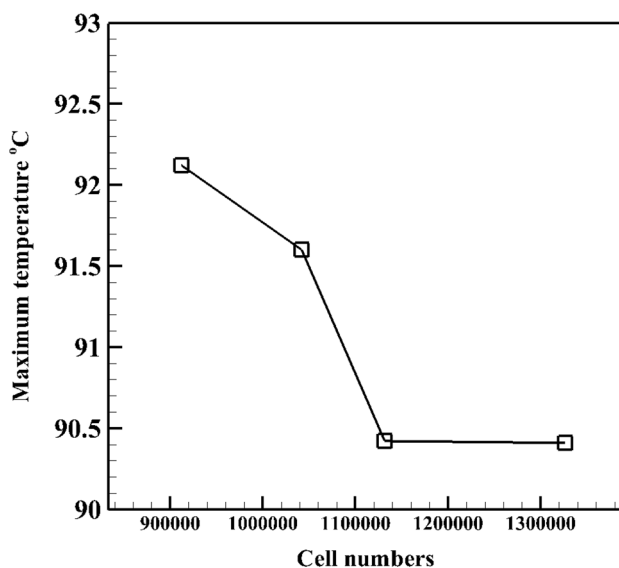**Fig. 8** Grid study for first step of simulation

Fig. 9 Grid study for second step of simulation

Fig. 10 Comparative receiving heat flux recent; CFD relative to Empirical and Ref [9]

particle concentration decrement resulted diminished divergence.

Similar to previous studies [9, 12, 13], since the recent study was performed on an industrial case, Figures are presented as a function of flow rate which is a more common parameter in industrial applications. Note that, though, due to the presence of various particle concentrations, thermophysical properties of nanofluid are not constant where results variable Reynolds number at a constant flow rate. While this paper is an industrial case study, some of the critical heat transfer parameters have been presented as a function of Reynolds number at the end of results.

For the purpose of hot spot marking, heat flux reception and temperature distribution on the outer hot-side of WCP are dedicated in Figs. 13 and 14 at 10.047 kg/s flow rate, respectively. Comparison of Figs. 13 and 14 with Fig. 12. [9] confirmed mechanical failures due to the thermal stresses which resulted from hot spots. Nevertheless, the areas close to the elbows and curved bindings are common places for hot spot induction because of magnificent receiving heat flux and low velocity stream due to the sizable vorticities. In the same way, an expanded hot area is beheld closet to the outlet where induced for the reason that a big vortex with very low velocity core near the outlet decreased convective heat transfer rate.

Further, various accurate simulations were conducted to evaluate influences of the change in the flow rate and nanoparticle concentrations including simulation at 9, 10, 11 and 12 kg/s flow rates for 3%, 4% and 5% of particle concentrations. Initially, as a critical parameter maximum temperature on WCPs outer hot-side has been presented in Fig. 15 for constant flow rates versus various particle concentrations as well as Fig. 16 for constant particle concentrations versus various mass flow rates. Based on Figs. 15 and 16 for all flow rates, at a constant flow rate, the maximum temperature decreased with concentration rise. Similarly, at a constant concentration, the maximum temperature dropped by increasing the flow rate. Additionally, constant flow rate diagram slopes increased upon reduction in the flow rate revealing that increment in concentration exerted a higher influence at lower flow rates. Subsequently, the results yielded the highest and lowest maximum temperature for pure water at 9 kg/s equivalent to 96.5558 °C and for 12 kg/s for 5% concentrated nanofluid equivalent to 76.1993 °C, respectively.

Likewise, the highest differences between maximum and averaged temperature on WCPs outer hot-side occurred at 9 kg/s for pure Water equivalent to 47.6681 °C
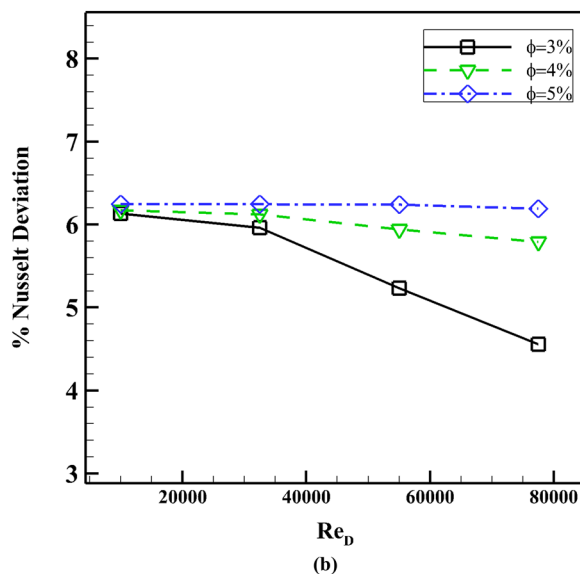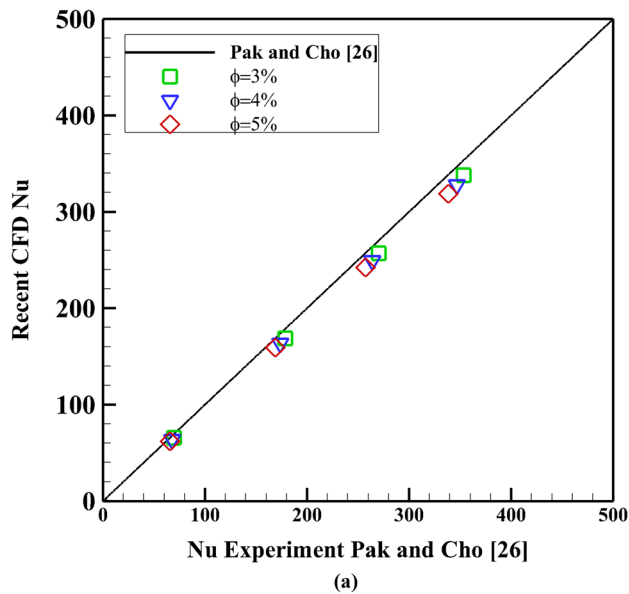
(a)

(b)

Fig. 11 Comparative Nusselt number (**a**) and Nusselt deviation (**b**) with experimental correlation Pak and Cho [26]

Fig. 12 Mechanical failure locations on WCPs hot-side [9]

and lowest at 12 kg/s for 5% concentration equivalent to 29.4546 °C. Based on Fig. 17, at a constant flow rate, the maximum and average temperature differences decreased by increasing the particle concentration. Since the maximum and average temperature difference constitutes a major reason of hot spot induction, the concentration and flow rate elevation led to reduced hot spot influences on the mechanical behavior of WCP. In other words, a decrease in the maximum and average temperature leads to smoother temperature distribution on the hot-side; thus, the thermal stresses produced from non-uniform thermal strains decreased causing less mechanical failure.

Notably, smoother temperature distribution occurred as a direct result of reduction in differences between local and average convective heat transfer coefficient yielding a uniform heat transfer.

Generally, different EAF cooling systems are divided into open circuit and closed-circuit cooling systems [5], where this investigated case includes a closed circuit cooling system. To examine the influence of nanofluid application on the whole integrated cooling system, Fig. 18 presents the WCPs outlet temperature at constant flow rates versus particle concentrations. Regard to the factory monitoring system, the inlet temperature for all simulations is assumed equivalent to 30.527 °C. In contrast to the maximum outer hot-side temperature, the outlet temperature increased by elevation of particle concentration at a constant flow rate. Since the simulation was conducted under steady state condition to WCP and the summation of heat flux received was constant for all simulations, the transferred heat was constant for all simulations. Hence, the differences between the outlet temperature occurred as a result of reduced specific heat capacities by increasing particle concentrations at a constant flow rate.

In addition, convective heat transfer coefficient (h (W/m^2 K)) is another effective parameter in thermal operation of WCPs, as studied in Fig. 19 for constant flow rates versus particle concentrations. The results presented in Fig. 19 revealed that elevation of the particle concentration led to a significant rise in the convective heat transfer coefficient as a result of elevated thermal conductivity of nanofluid with the growth of concentration. On the other hand, the increase in heat transfer led to reduced average hot-side temperature, explaining the heat losses in EAF studied as a ratio of h_{eff}/h and presented in Fig. 20. It illustrates that the particle concentration increment resulted in reduced h_{eff}/h. Indeed, the rise in particle concentrations affected

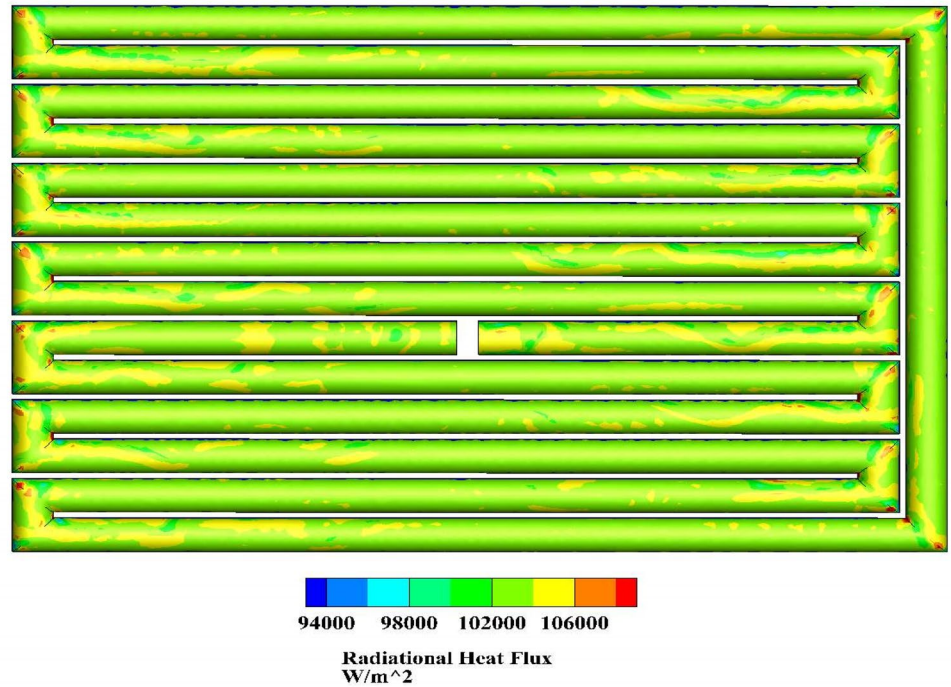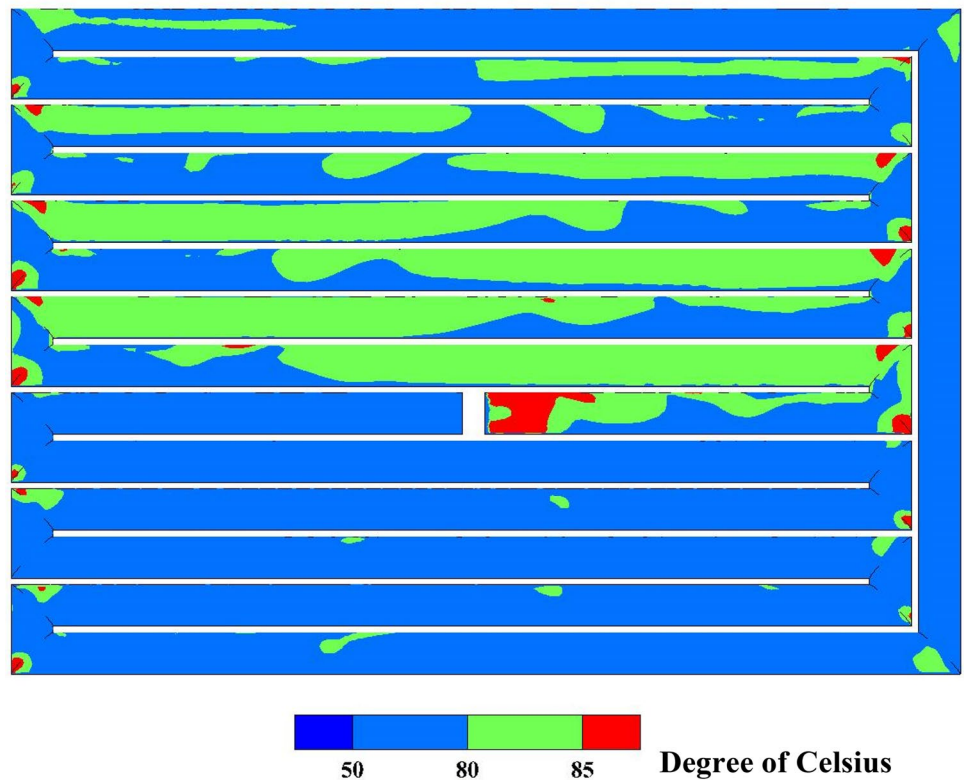**Fig. 13** CFD result of receiving heat flux distribution on the hot-side of WCP

Fig. 14 CFD result of temperature distribution on WCP hot-side (degree of Celsius)

the convective heat transfer coefficient more at lower flow rates. Accordingly, the highest and the lowest values for h_{eff}/h occurred at 9 kg/s (which is the lowest flow rate) and 5% concentration equivalent to 1.175959, 12 kg/s and 3% concentration equivalent to 1.05081, respectively. Notably, the increase in the momentum transport with the flow rate elevation produced stronger convective effects; thus, the impact of conductivity increment on heat
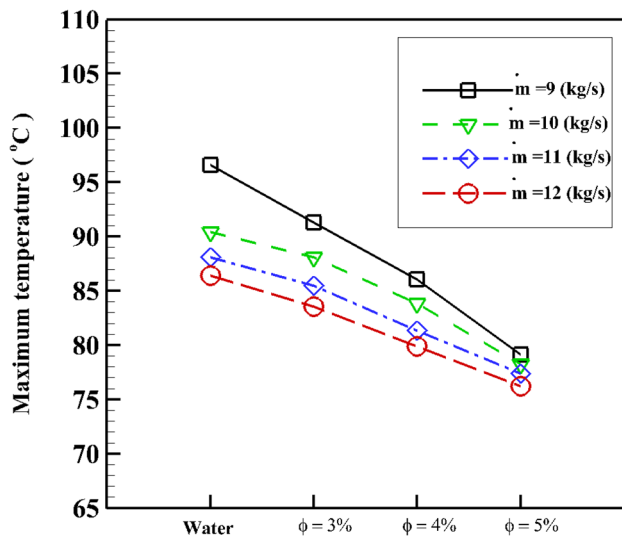
Fig. 15 Maximum temperature on WCP hot-side at constant flow rates vs concentration
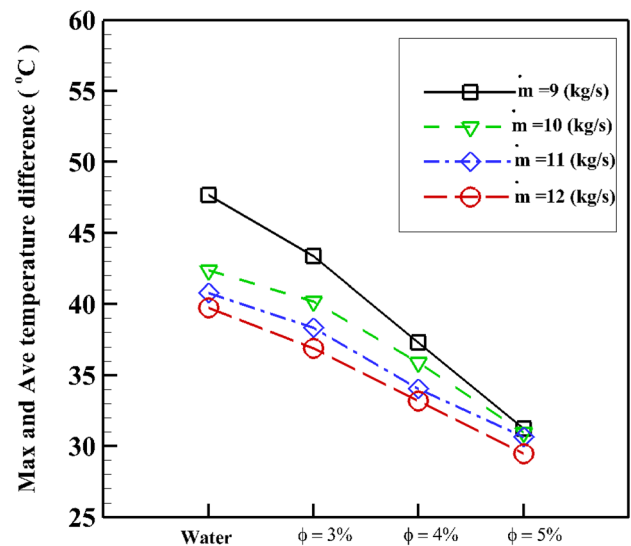
Fig. 17 Difference between maximum and averaged temperature on WCP hot-side
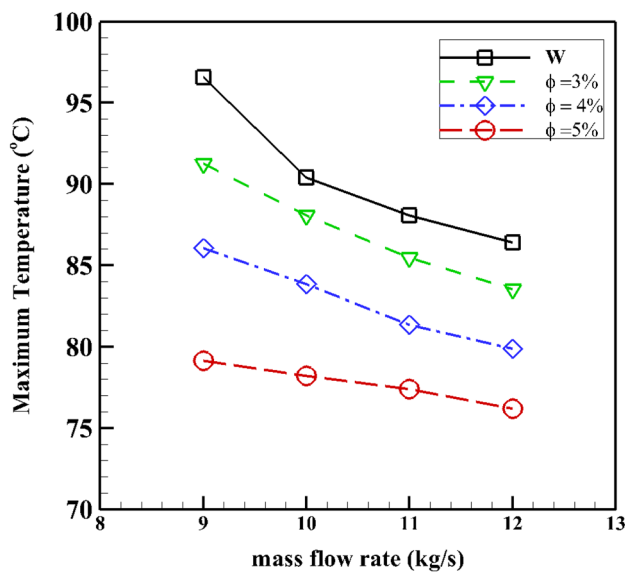
Fig. 16 Maximum temperature on WCP hot-side at constant concentration vs flow rate
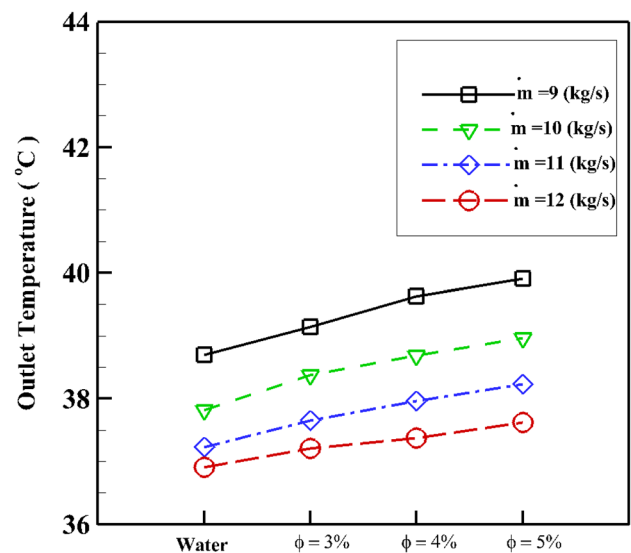
Fig. 18 Outlet temperature of WCP at constant flow rate vs concentration

transfer phenomena dropped significantly. Conversely, Nusselt number (Nu) which is another effective thermal performance parameter, decreased with the rise of particle concentrations at a constant flow rate as presented in Fig. 21. On the other hand, with particle concentration elevation, Nu diminished due to the reduction in Reynolds and Prandtl Numbers.

Further, the temperature contours on the WCPs hot-side are presented in Fig. 22 at 10.047 kg/s and various particle concentrations. Based on Fig. 22, not only higher value

contours have obviously covered the surface of hot-side when the coolant was pure water, but also the hot spots expanded into a wider area of hot-side. The particle concentration rise yielded a smoother temperature distribution as well as a lower maximum and average temperature on the hot-side as confirmed by Figs. 15, 16, and 17. Furthermore, increment in the particle concentration faded hot area coverage and drove them only at the elbows and bends occurring as a result of increased local convective heat transfer rate and reduced averaged and local h difference over the hot-side.
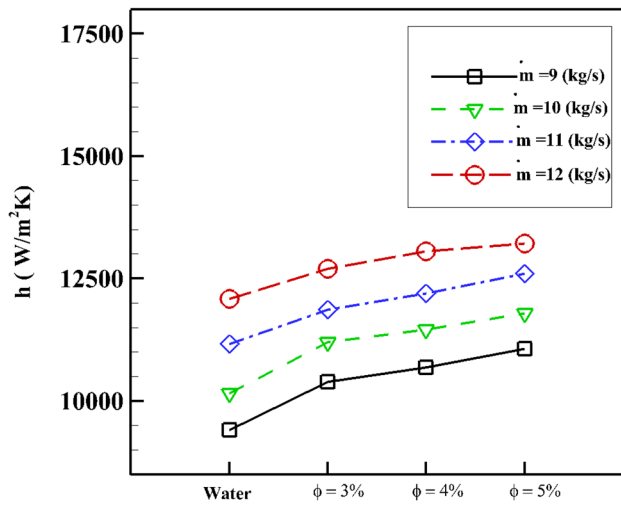
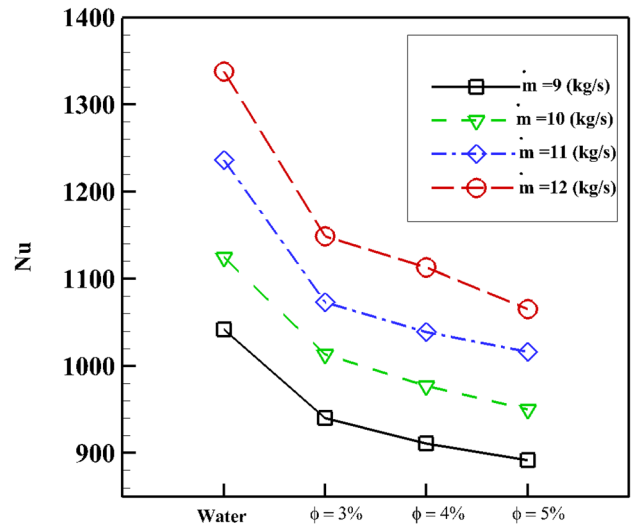**Fig. 19** Convective heat transfer at constant flow rate vs concentration

Fig. 21 Nusselt number at constant flow rate vs concentration
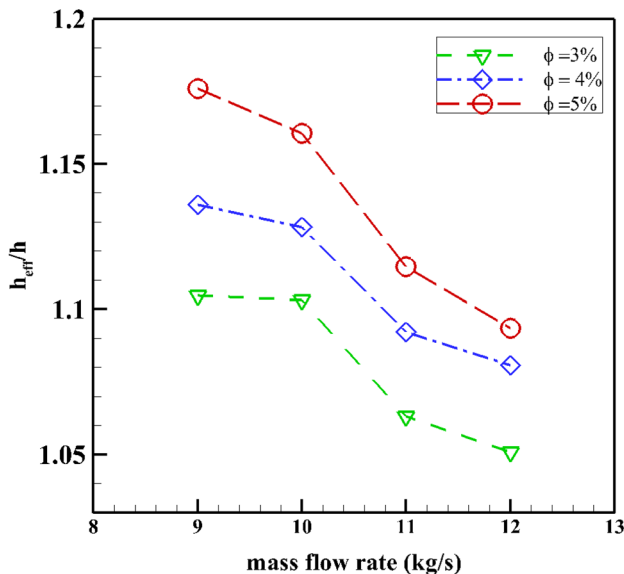

Fig. 20 Convective heat transfer coefficient ratio at constant concentration vs flow rate

Figure 23 illustrates the temperature distribution on the symmetrical plane of WCP at 10.047 kg/s flow rate and various concentrations. Accordingly, the patterns of coolant fluid temperature changes are almost the same, though the higher concentration led to a wider high temperature zone because of augmentation of heat transfer with the increment in concentration. Similarly, Fig. 24 shows the velocity magnitude contours on the symmetrical plane of WCP at 10.047 kg/s flow rate and for pure water and 5% concentration. Although the velocity patterns are almost similar, low velocity areas are wider for the

5% concentration. Since the concentration increment led to increased viscosity, the flow areas affected by viscous area are wider at the 5% concentration. In other words, the increase in viscosity naturally led to diminished velocity magnitude in viscous flow areas.

Figure 25 displays the streamlines in the presence of velocity magnitude contours in the symmetrical plane of the WCP for pure water at 10 kg/s flow rate, revealing the direction of fluid particle motion. According to Fig. 25, in areas with high velocity, the flow pattern is axial. Inspecting the streamlines in the bends and elbows presented in Fig. 26, it can be clearly seen that in the low-velocity zones, some vortices exist causing the appearance of extremely low velocity spots in the center of the vortices near the bends. These low velocity areas develop hot spots due to diminished local convective heat transfer on the hot-side surface. These hot spots can be reduced by increasing the conductivity of the coolant fluid. The increase in thermal conductivity is due to the elevation of the nanofluid concentration of the base fluid, which is why the temperature distribution of the hot spots declined and temperature distribution became more uniform with the concentration increment.

Above all, for academic aspects Fig. 27 presents the maximum WCPs hot-side temperature as a function of Reynolds number Re_D at constant concentrations. Based on the results, at a constant concentration, the rise in Re_D led to diminished maximum temperature of the hot-side. Using Vertical lines in Fig. 27, illustrates that for a constant Re_D, the particle concentration increment led to reduced maximum temperature on the hot-side. Accordingly, the highest and lowest maximum temperatures occurred at $Re_D = 230,810$, equivalent to 96.5558 °C and $Re_D = 307,747$, equivalent to 76.1993 °C, respectively. Similarly, as dedicated in Fig. 28, the
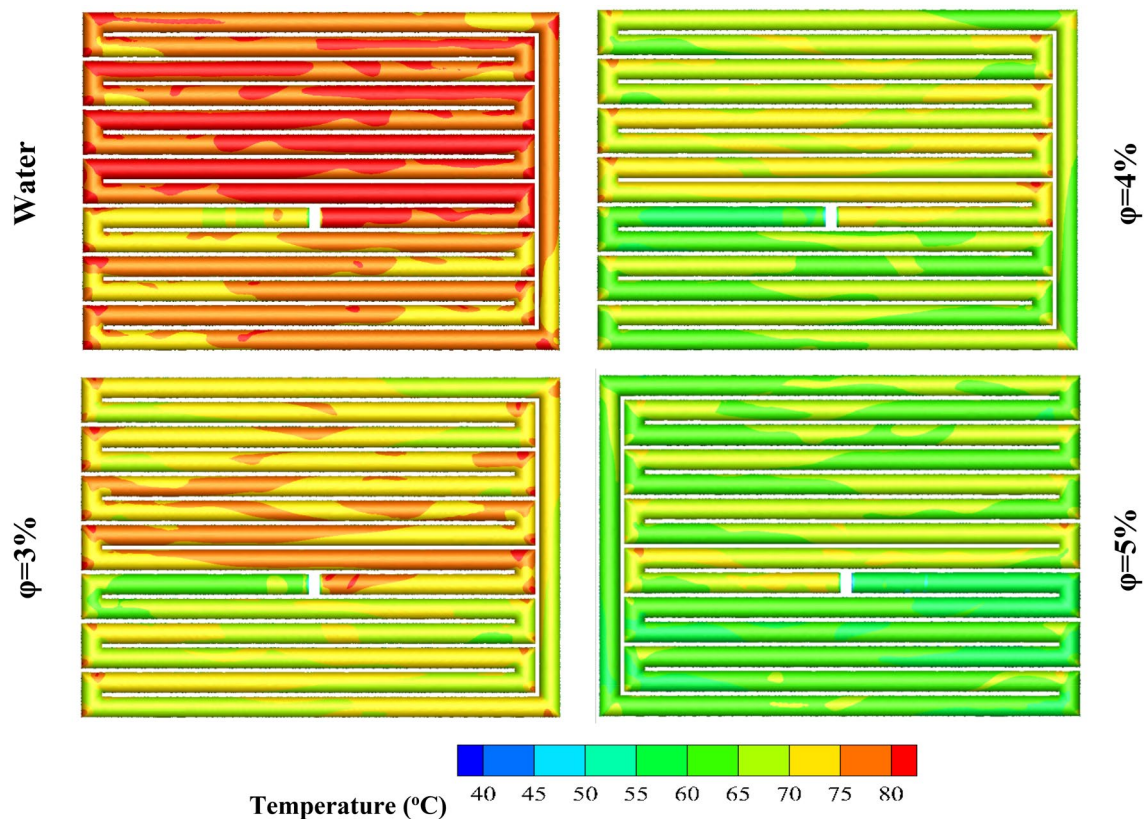
Fig. 22 Temperature distribution on WCP hot-side (Celsius)

differences between the maximum and average temperature on the WCPs hot-side decreased with elevation of the Re_D number except for 5% concentration which is almost constant and independent of Re_D number as also noticed in previous studies [22]. Using a vertical line in Fig. 28 revealed that increment in Re_D resulted lowered maximum and average temperature on the hot-side. Finally, the h_{eff}/h ratio function of Re_D for constant concentrations is illustrated in Fig. 29. Based on the results, for a constant concentration, rise in Re_D led to reduced h_{eff}/f. The maximum and minimum values for h_{eff}/h were accurately calculated as 1.17596 and 1.05081 corresponding to $Re_D=230{,}810$ at 3% concentration and $Re_D=285{,}191$ at 5% concentration, respectively.

4 Conclusion

In this study, computational fluid dynamics simulation was conducted to an electric arc furnace wall water cooling panel located in Isfahan steel company in two steps while considering the real condition using water for validation and Al_2O_3/Water nanofluid at 3%, 4%, and 5% particle concentrations to evaluate thermal performance of WCP. After accurate and numerous validations, the maximum

temperature, differences between maximum and averaged temperature, and temperature distribution on WCPs hot-side were calculated for 3%, 4%, and 5% concentrations and flow rates between 9 and 12 kg/s. The findings can be summarized as follows:

- At steady state and assuming that electric arc is off, receiving heat flux to the hot-side was equivalent to 103,678 W/m2K which was calculated 4% higher than the real empirical condition. This confirmed that geometrical simplification has a minor effect on the calculated receiving heat flux.
- Heat flux exposure and temperature distribution on the hot-side of WCP confirmed that hot spots were induced near the elbows and bends.
- The highest maximum temperature on the hot-side was calculated 96.55 °C for 9 kg/s with pure water coolant while the lowest maximum temperature was found 76.2 °C for 12 kg/s and 5% concentration which showed 21% differences.
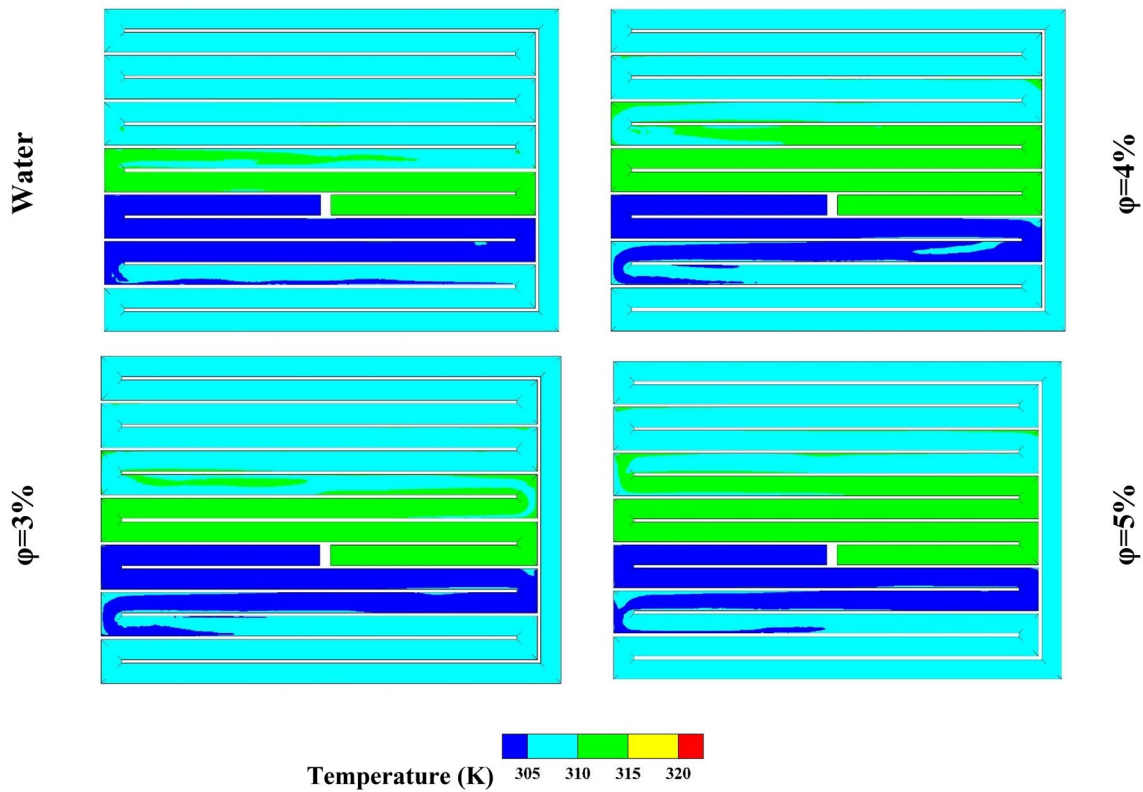
Fig. 23 Temperature distribution on symmetrical plan of WCP (K)
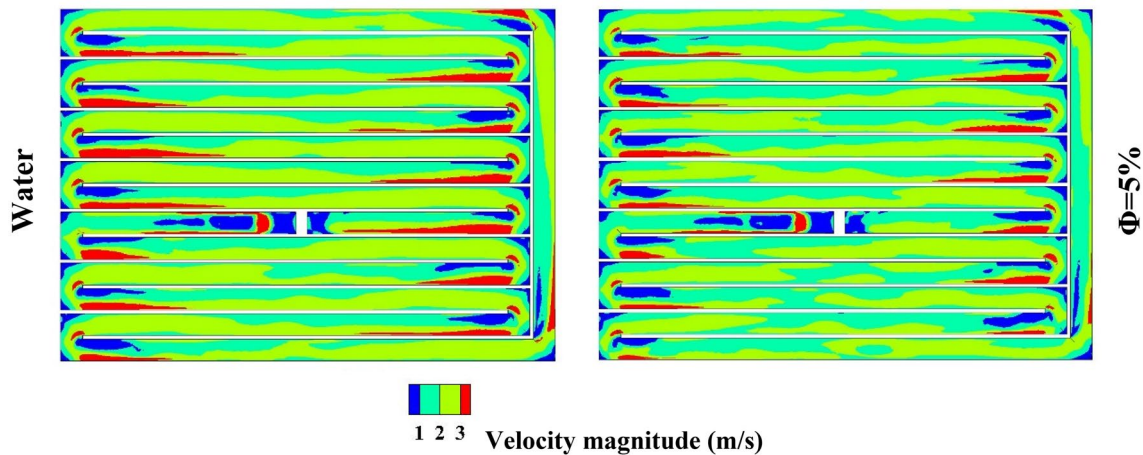

Fig. 24 Velocity magnitude contours on symmetrical plan of WCP at 10 kg/s (m/s)

- At the nominal flow rate 10.047 kg/s, the average temperature on the hot-side decreased by 1.87%, 2.87, and 2.97 for 3%, 4%, and 5% particle concentrations relative to pure water, respectively.
- Differences between the maximum and averaged temperature on the hot-side dropped by 2% to 12% upon alteration of particle concentration from 3 to 5% at 10.047 kg/s flow rate.
- The outlet temperature of the cooling fluid increased by 1.45%, 2.29%, and 3.03 for 3%, 4%, and 5% particle concentration relative to pure water at 10.047 kg/s, respectively.

Fig. 25 Streamlines and velocity contours on symmetrical plan at 10.047 kg/s
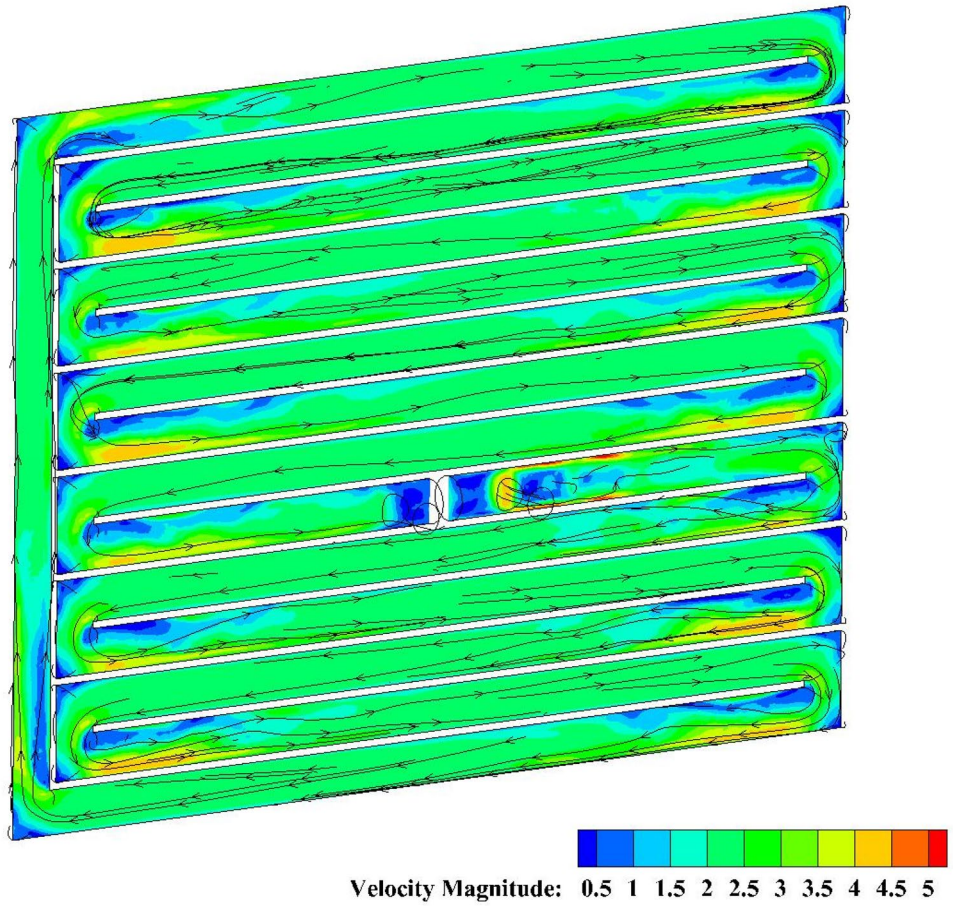
Fig. 26 Detailed streamlines near the elbows and bends at 10 kg/s
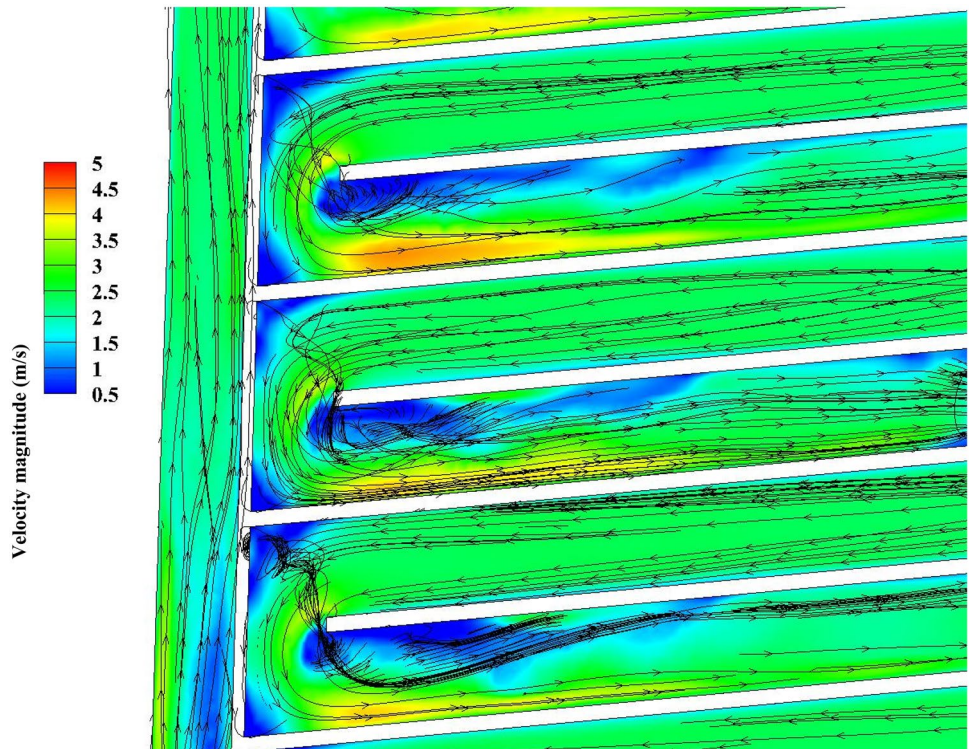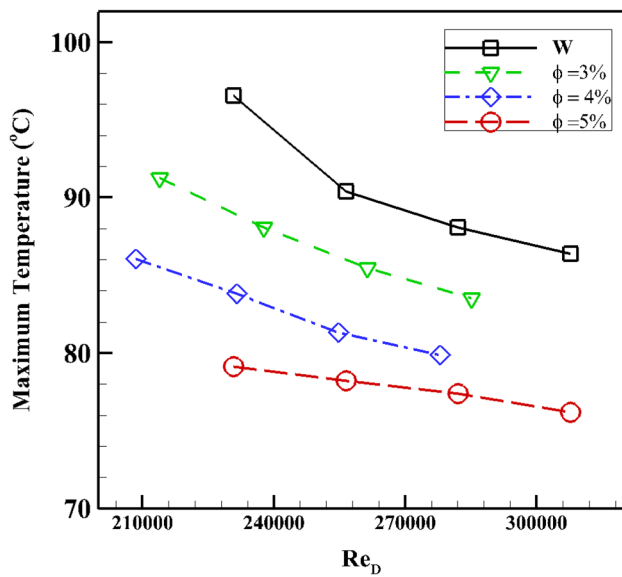
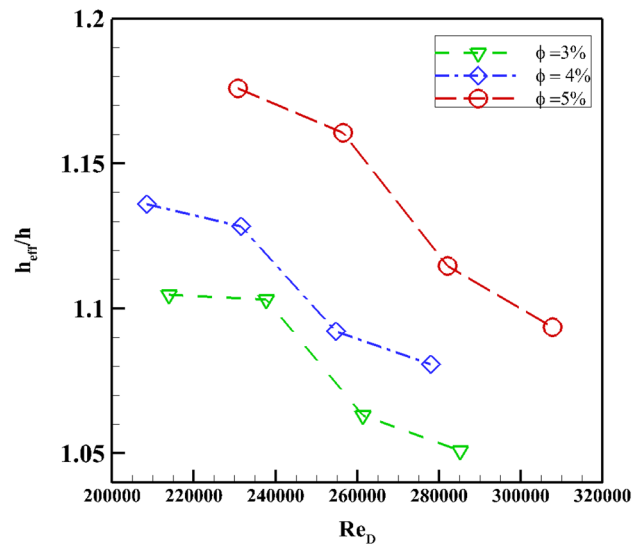**Fig. 27** Maximum temperature on WCP hot-side at constant concentration vs Re_D

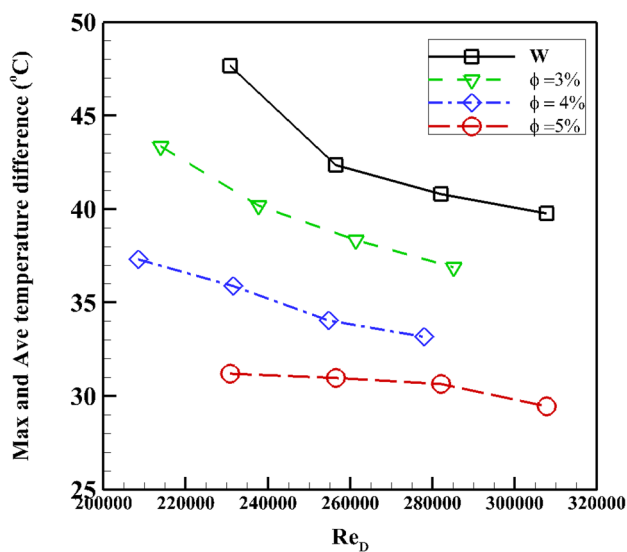**Fig. 29** Convective heat transfer ration at constant concentrations vs Re_D

Fig. 28 Difference between maximum and averaged temperature on WCP hot-side at constant concentration vs Re_D

- Convective heat transfer coefficient increased by 10.3%, 13.1%, and 16.05% for 3%, 4%, and 5% particle concentrations relative to pure water, respectively.

It is worth noting that in this study, although the electrodes at the refining stage have been lifted up, a small portion of electrodes remain in the EAF, which may affect the heat flux distribution on the panels that can be taken into account in a future study. A transient state of the EAF can also be considered during the melting process. Furthermore, the performance of other nanofluids may be estimated by considering them as a coolant of a WCP.

Author contributions First author has applied numerical simulations under the supervision of second and third author. Also all graphical results have been derived by first author. The initial draft of manuscript has been written by first author and reviewed by second and third. The operational data from factory has been collected by forth author. All authors have read and approved final manuscript.

Data availability Parts of the data and materials are available upon the request.

Declarations

Competing interests This work was not influenced by any known competing financial interests or personal relationships of the authors.

References

1. Manana M (2021) Increase of capacity in electric arc-furnace steel mill factories by means of a demand-side management strategy and ampacity techniques. Int J Electr Power Energy Syst 124:106337

2. Patry PG, Harry M (1998) The making, shaping and treating of steel 11th edition steelmaking and refining volume. The AISE Steel Foundation

3. Simoes JP, Pfeifer H, and Kirschen M (2005) Thermodynamic analysis of EAF electrical energy demand. In: 8th European electric steelmaking conference, England, pp 113–119

4. Themelis NJ, Szekely J (1971) Rate phenomena in process metallurgy. Wiley, New York

5. Ghasemi SE (2017) Forced convective heat transfer of nanofluid as a coolant flowing through a heat sink: experimental and numerical study. Mol Liquids 248:264–270

6. Kilkis IB (1994) "A simplified model for radiant heating and cooling panels", simulation practice and theory. Simul Pract Theory 2:61–76

7. Logar V (2012) Modelling and validation of an electric arc furnace: part1, heat and mass transfer. ISIJ Int 52:402–412

8. Henning B (2010) Evaluating AC and DC furnace water cooling system using CFD analysis. Engineering Aspects-Furnaces congress, pp 849–856

9. Mombeni AG (2015) Transient simulation of conjugate heat transfer in the roof cooling panel of electric arc furnace. Appl Therm Eng 98:80–87

10. Yigit C (2015) CFD modelling of carbon combustion and electrode radiation in an electric arc furnace. Appl Therm Eng 90:831–837

11. Guo D (2003) Modelling of radiation intensity in an EAF. In: Third international conference on CFD in the mineral and process industries, Australia

12. Khodabandeh E (2017) Experimental and numerical investigations on heat transfer of water-cooled lance for blowing oxidizing gas in an electrical arc furnace. Energy Convers Manage 148:43–56

13. Khodabandeh E (2017) Parametric study of heat transfer in an electric arc furnace and cooling system. Appl Therm Eng 123:1190–1200

14. Ahmadi AA, Bahiraei M (2021) Thermohydraulic performance optimization of cooling system of an electric arc furnace operated with nanofluid: a CFD study. J Clean Product 310:127451

15. Yao C, Jiang Z, Zhu H, Pan T (2022) Characteristics analysis of fluid flow and heating rate of a molten bath utilizing a unified model in a DC EAF. Metals 12(3):390

16. Luo Q, Chen Y, Abraham S, Wang Y, Petty R, Silaen AK, Zhou C (2022) Effects of EAF operations on water-cooling panel overheating. Steel Res Int 93:2100844

17. Jabbari F, Rajabpour A, Saedodin S (2017) Thermal conductivity and viscosity of nanofluids: a review of recent. Chem Eng Sci 174:67–81

18. Pandya NS, Shah H, Molana M, Tiwari AK (2020) Heat transfer enhancement with nanofluids in plate heat exchangers: a comprehensive review. Eur J Mech B 81:173–190

19. Bahiraei M, Rahmani R, Yaghoobi A, Khodabandeh E, Mashayekhi R, Amani M (2018) Recent research contributions concerning use of nanofluids in heat exchangers: a critical review. Appl Therm Eng 133:137–159

20. Islam MR (2016) Nanofluids to improve the performance of PEM fuel cell cooling systems: a theoretical approach. Appl Energy 178:660–671

21. Sahota L (2017) Analytical characteristic equation of nanofluid loaded active double slope solar still coupled with helically coiled heat exchanger. Energy Convers Manage 135:308–326

22. Nayerdinzadeh Sh (2020) Experimental and numerical evaluation of thermal performance of parabolic solar collector using water/Al_2O_3 nanofluid: a case study. Int J Thermophys 41:59

23. Hosseini SM (2016) Performance of CNT-water nanofluid as coolant fluid in shell and tube intercooler of LPG absorber tower. Int J Heat Mass Transf 102:45–53

24. ANSYS Fluent, Theory Guide, 19

25. Allahyar HR (2016) Experimental investigation on thermal performance of a coiled heat exchanger using a new hybrid nanofluidnanofluid. Exp Thermal Fluid Sci 76:324–329

26. Pak BC, Cho YI (1998) Hydrodynamic and heat transfer study of dispersed fluids with submicron metallic oxide particles. Exp Heat Transf 11(2):151–170

27. Bejan A (2004) Convection heat transfer. Wiley, New York